Creep of aluminum syntactic foams

Olivier Couteau [1], David C. Dunand [*]

Department of Materials Science and Engineering, Northwestern University, 2220 Campus Drive, Evanston, IL 60208-3108, USA

Abstract

Aluminum syntactic foams with densities of 1.2–1.5 g/cm^3 were deformed at 500 °C under constant uniaxial compressive stresses ranging from 5 to 14 MPa. The foam creep behavior is characterized by a short primary stage and a long secondary stage where the strain rate is constant and minimum, followed by a tertiary stage at high stresses. The minimum strain rate varies with stress according to an apparent stress exponent n with a low value ($n \approx 1$) for stresses below 8 MPa, and a high value ($n \approx 14$) above 8 MPa. Finite-element modeling provides predictions for the foam strain rates that are in qualitative agreement with experimental results. Modeling also shows that the matrix transfers load to the ceramic elastic spheres, explaining the exceptionally high creep resistance of these syntactic foams as compared to aluminum foams without ceramic spheres. Modeling finally reveals that stresses vary with position in the matrix and time during creep, and that the onset of tertiary stage is associated with the appearance of sharp stress concentrations in the matrix.

1. Introduction

Syntactic metallic foams consist of hollow spheres surrounded by a metallic matrix [1] and are usually produced by metal infiltration of a packed preform of ceramic (or metallic) hollow spheres with sub-millimeter size [2–13]. The hollow nature of the spheres provides two functions. First, the empty space within the spheres produce closed pores, which encompass up to ~60 vol.% of the total foam volume, depending on sphere packing efficiency and wall thickness. Second, the ceramic shells create a percolating, continuous skeleton within the foam, resulting in enhanced strength and stiffness as compared to unreinforced foams with the same average density.

In previous studies, Balch et al. [10,11] studied the ambient-temperature compressive properties of syntactic aluminum foams containing hollow silica-mullite spheres and discussed their compressive stiffness, strength, damage properties and energy absorption in terms of load transfer between the matrix and the spheres. The same aluminum syntactic foams previ-

ously examined by these authors at ambient temperature are investigated in the present study at elevated temperature. The compressive creep rate is measured for various constant uniaxial stresses (ranging from 5 to 14 MPa) at temperatures as high as 500 °C (corresponding to a homologous temperature of 0.83). Finite-element modeling (FEM) is carried out on simplified periodic and quasi-periodic models and compared with the experimental creep results.

2. Experimental procedures

We use aluminum syntactic foams cut from the same billet produced for a previous investigation; experimental procedures for foam fabrication are described in details in the original references [10,11] and are summarized here briefly. Hollow silica-mullite spheres with 15–75 μm diameter and 2–5 μm wall thickness (provided by Envirospheres PTY Ltd.) were tap-packed into a preform which was pressure infiltrated with molten aluminum of commercial purity at 710 °C. The solidified billet was then cut into parallelepiped specimens with 7 mm × 3 mm × 3 mm dimensions whose densities were measured by helium pycnometry.

Constant-load compressive creep tests were conducted on these specimens in air at temperature between 250 and 500 °C and for engineering stresses ranging from 1 to 14 MPa. Creep

* Corresponding author.
  E-mail address: dunand@northwestern.edu (D.C. Dunand).
[1] Current address: European Commission, Institute for Reference Materials and Measurements, Retieseweg 111, B-2440 Geel, Belgium.

deformation was significant only at temperature above 325 °C and for stresses above 5 MPa. Thus, creep results are presented here only for the highest temperature of 500 °C and for stresses above 5 MPa. For all samples, a total cumulative engineering strain of 5% was not exceeded unless, in a few cases, fracture of the specimen was the goal. A direct-loading compression creep machine was used under constant-load condition. The engineering strain was calculated from cross-head displacement data measured continuously by a linear voltage displacement transducer.

3. Experimental results

The foam specimens displayed a density in the range 1.23–1.48 g/cm^3, corresponding to relative densities of 0.46–0.55 (as compared to pure aluminum) and a sphere volume fraction $f = 59$–71% (using a density of 0.62 g/cm^3 for the spheres, as measured by Ref. [11]). Foams showed a uniform spatial distribution of spheres, good aluminum infiltration of the volume between spheres and few fragmented or infiltrated spheres, as illustrated in Fig. 1. As reported previously [11], the sphere walls are porous and of varying thickness.

Fig. 2(a and b) shows creep curves measured for foams tested at 500 °C for stresses between 5 and 13 MPa. All curves exhibit a primary creep stage with continuously decreasing strain rate, followed by a secondary stage where the average strain rate is constant (strain fluctuations on the creep curves of Fig. 2(a and b) were due to small thermal fluctuations in the creep furnace). Finally, for stresses above 9 MPa (Fig. 2(b)), a tertiary stage characterized by increasing strain rates appears after relatively short times and this stage is usually associated with severe damage in the foams visible as crush bands and wrinkled specimen sides. By contrast, for stresses below 9 MPa, no tertiary stage is observed, even after very long testing times of about 1 week (6×10^5 s, not represented in Fig. 2(a) extending to 1×10^5 s).

4. Modeling

The structure of syntactic foams is too complex to permit simple analytical models of the type developed for creep of reticulated single-phase foams, which is based on strut bending and compression [14,15]. Thus, FEM was carried out using the commercial ABAQUS package [16]. Such a numerical approach has also the advantage, as compared to analytical modeling, to provide spatially and time-resolved information on the stress distribution within the foam.

Unit cells consisting of aluminum matrix containing fully bonded hollow spheres were used. Periodic boundary conditions, where the faces of the unit cell are kept flat and parallel

Fig. 2. Creep strain as a function of time measured for foams (with volume fractions $f = 59$–71%, indicated next to each curve) deformed at 500 °C for compressive stresses: (a) below 9 MPa and (b) above 9 MPa.
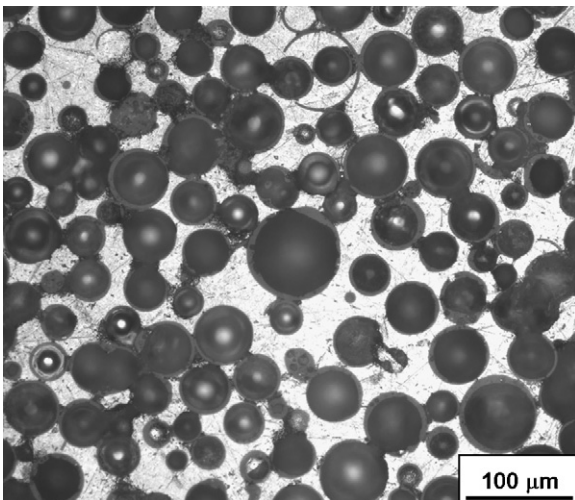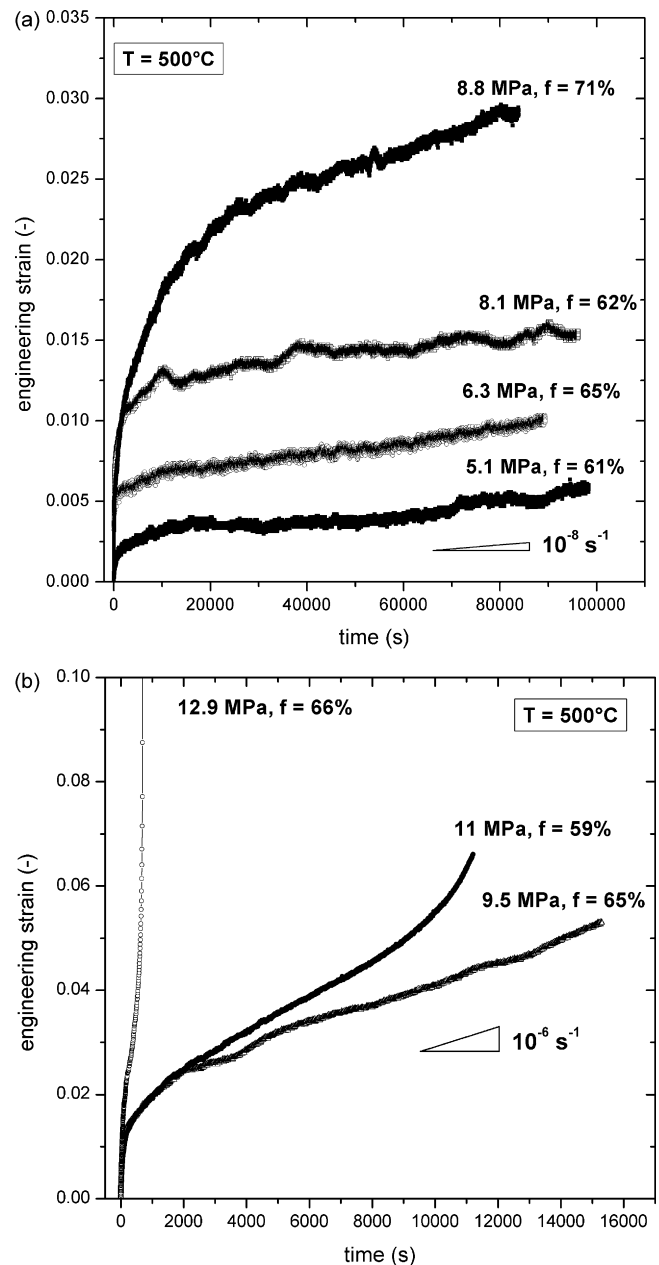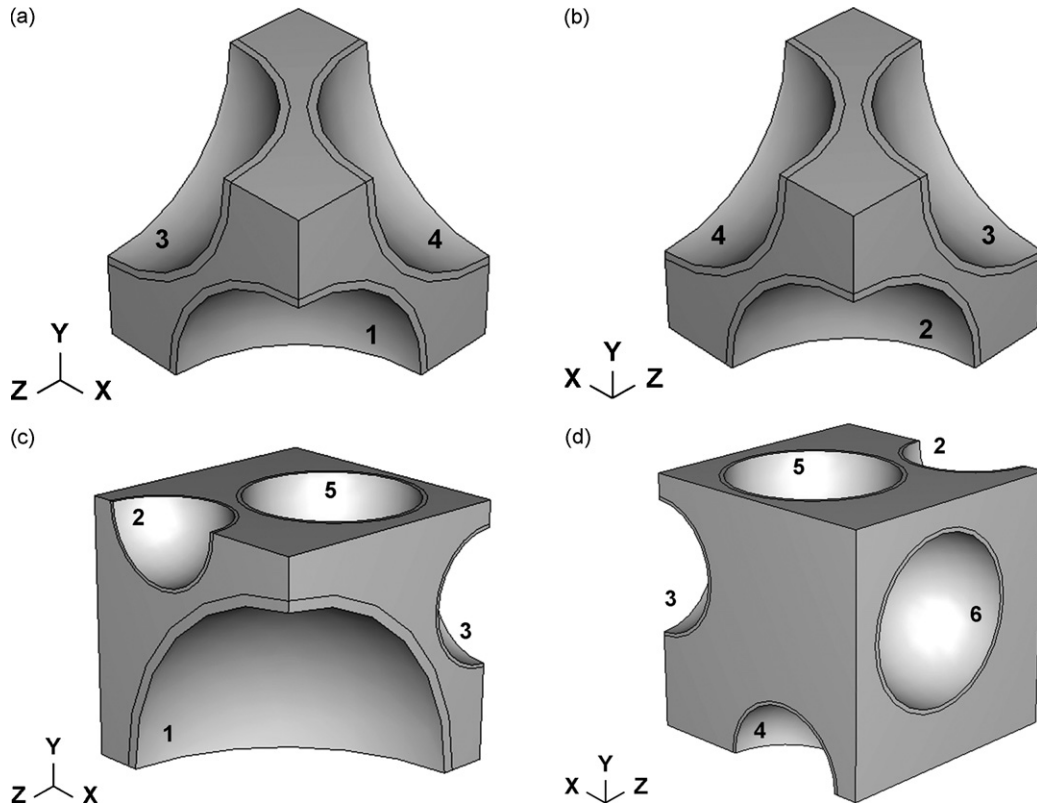
Fig. 1. Micrograph of metallographic cross-section for syntactic foam, showing ceramic hollow microspheres and pure aluminum matrix.

Fig. 3. Unit cells used for FEM: (a) face cubic centered (FCC) sphere arrangement with sphere volume fraction $f = 65\%$; (b) as (a) but rotated $180°$ around the Y axis; (c) pseudo-random (PR) sphere arrangement with $f = 55\%$; and (d) as (c) but rotated $180°$ around the Y axis. Uniaxial compressive stress is applied along one of the main axes.

in the three orthogonal space directions, allowed to simulate a foam of infinite dimensions, thus capturing the interaction of neighboring spheres. Two types of periodic arrangement of spheres were created: face cubic centered (FCC) and pseudo-random (PR), the latter corresponding to a random arrangement of spheres in the unit cell which is repeated periodically in the three directions of space. As illustrated in Fig. 3(a and b), the FCC unit cell contains four sphere sections (each with 1/8 the volume of a full spheres) and the PR unit cell contains six sphere sections (with $(1/8) - (1/2)$ volume). The sphere radii for both models are given in Table 1. For both models, the ratio between the sphere wall thickness and the sphere radius was taken as 0.05 (1:20). This wall thickness is lower than that in the experimental foams, a discrepancy expected to have a negligible effect on the

matrix stress distribution. In both PR and FCC cases, the volume fraction of spheres was maximized while maintaining a large enough volume of matrix between spheres to achieve accurate meshing. The FCC model, being more close-packed in geometry, thus achieved a higher sphere volume fraction ($f = 65\%$) than the PR model ($f = 55\%$).

The creep strain was calculated from the difference in unit cell dimension along the loading Y axis. The unit cells were meshed by 10 nodes quadratic tetrahedral elements. Typically, a model consists of ~25,000 such elements. The ceramic wall material in the hollow spheres was considered to be elastic with a Young's modulus of 125 GPa [11]. The pure aluminum matrix was assumed to deform elastically with a Young's modulus of 49 GPa at $500°C$ [17], as well as by creep according to a power-law, where the uniaxial creep strain rate $\dot{\varepsilon}$ is given by

$$\dot{\varepsilon} = A\sigma^n \tag{1}$$

where σ is the stress, $A = 3.95 \times 10^{-8}\,MPa^{-4.4}\,s^{-1}$ is a temperature-dependent constant calculated at $500°C$ from data provided in Ref. [18] and $n = 4.4$ is the stress exponent [18]. Primary creep of the matrix was ignored.

Fig. 4 shows creep curves calculated for an applied stress of 5.1 MPa at $500°C$ for both FCC and PR cells (with $f = 65$ and 55%, respectively). Similar to the experimentally measured creep curves (Fig. 2(a and b)), the calculated creep curves exhibit a primary region where strain rates decrease with time, followed by a secondary region where the strain rate is near constant.

Table 1
Sphere dimensions for the face cubic centered (FCC) and pseudo-random (PR) arrangements, expressed as ratio between sphere outer radius R and unit cell size a

Sphere number	Fraction of full sphere	R/a (−)
FCC arrangement		
1, 2, 3, 4	1/8	0.677
PR arrangement		
1	1/8	0.848
2, 3, 4	1/4	0.272
5, 6	1/2	0.344

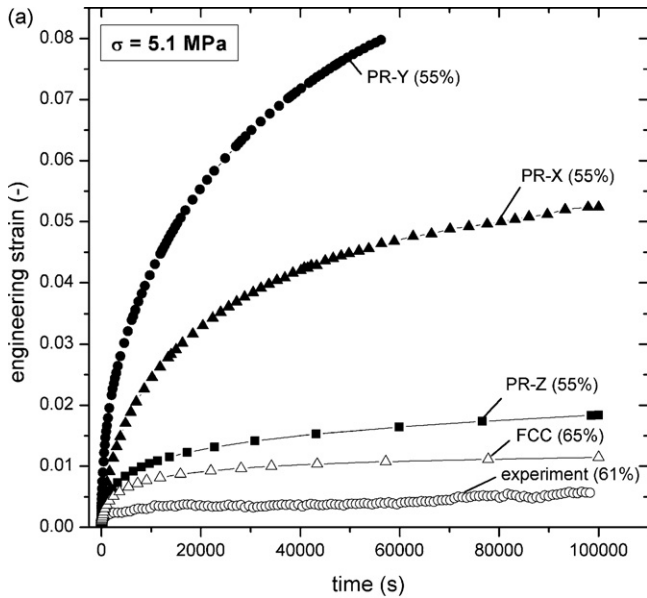Sphere numbers are indicated in Fig. 3.

Fig. 4. Creep strain as a function of time obtained by FEM for FCC sphere arrangement (f = 65%) and PR sphere arrangement (f = 55%) at 500 °C for a compressive stress of 5.1 MPa. Curves for PR arrangement are shown for deformation along the three main axes. For comparison, the corresponding experimental foam creep curve is also plotted for a foam with f = 61%.

Also shown in Fig. 4 are creep curves for the PR geometry subjected to the same stress applied along the other two axes (X and Z axes). It is apparent that both the primary creep and the secondary creep rate are affected by the loading direction. In Fig. 4, the creep curve experimentally measured on a foam shown in Fig. 2a (f = 61%) is also given for comparison: the FCC calculated curve is closest to the experimental results, both in terms of primary and secondary creep strain.

In Fig. 5, calculated creep curves for the FCC arrangement at 500 °C are shown for various stresses. For all curves, the
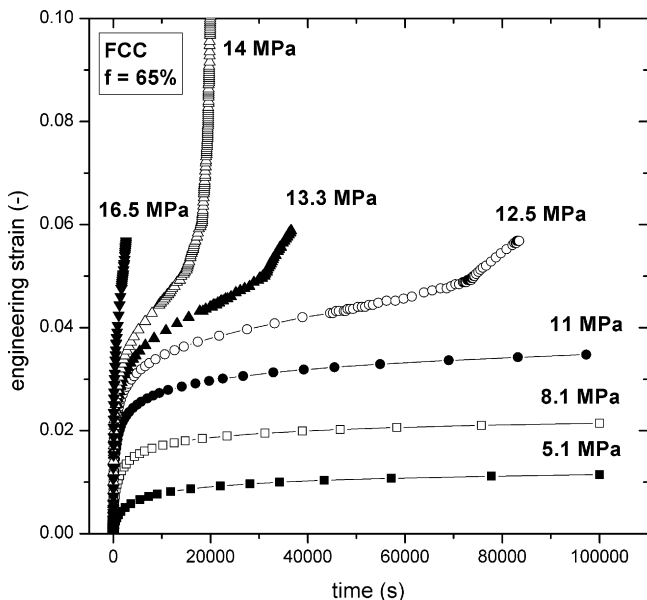

Fig. 5. Creep strain as a function of time obtained by FEM for foams with FCC sphere arrangement (f = 65%) for various compressive stresses at 500 °C.
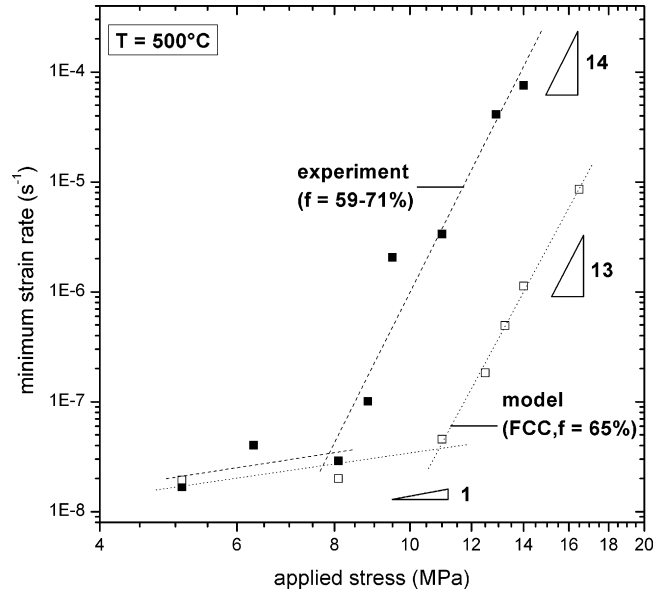

Fig. 6. Minimum strain rate as a function of applied compressive stress as determined by FEM for FCC sphere arrangement (f = 65%), and as measured experimentally on syntactic foams (f = 59–71%).

total accumulated primary creep strain and the secondary creep rate increase with increasing stress. As for the experimentally measured foams plotted in Fig. 2(a and b), the creep behavior of the FCC foams can be divided in two regimes: (i) for stresses below 11 MPa, no tertiary stage is visible; (ii) for stresses above 11 MPa, a tertiary stage is present, starting at shorter times as the applied stress increases.

5. Discussion

5.1. Comparison with continuum models

Fig. 6 shows a double-logarithmic plot of minimum state strain rate measured on foams (f = 59–71%) as a function of applied stress. As for the experimental creep curves shown in Fig. 2(a and b), two regimes can be distinguished. Below 8 MPa, the apparent stress exponent (i.e., the slope of the best-fit line in Fig. 6) is close to unity. Above 8 MPa, the minimum strain rate increases much more rapidly with the applied stress, leading to an apparent stress exponent close to 14. In the low-stress regime, the minimum strain rates are in the range 10^{-8} to 10^{-7} s^{-1}, which is about six orders of magnitude smaller than the minimum, secondary strain rate for pure aluminum at the same stresses and temperature, calculated assuming deformation by dislocation power-law [18]. Furthermore, aluminum foams without reinforcement are expected to creep faster than pure aluminum by a factor F, dependent on the relative density ρ^*/ρ_s (where ρ^* is the foam density and ρ_s is aluminum density). For a model considering bending of struts by creep [19], this factor takes a value $F = 33(\rho^*/\rho_s)^{-7.1}$ (using n = 4.4 for aluminum), while for a model assuming creep compression of struts [14], the factor is $F = 126(\rho^*/\rho_s)^{-4.4}$. For an aluminum foam with the same relative density (ca. ρ^*/ρ_s = 0.50) as our syntactic foams, the factor F is then in the range 2700–4500. Thus, for stresses

below 8 MPa, the creep rate of the syntactic aluminum foams is slower by over nine orders of magnitude as compared to a hypothetical unreinforced aluminum foam of the same relative density. Even for the highest stress measured here, the syntactic foams have creep rates more than four orders of magnitude lower than calculated for an unreinforced aluminum foam. This remarkable improvement in compressive creep response is due to the presence of the reinforcing spheres which affect creep by two mechanisms, as in cast metal matrix composites with large (>100 μm) monolithic spheres: (i) the reinforcement constrains matrix flow and (ii) the reinforcement carries a comparatively large portion of the applied stress, due to the load transfer effect examined by Balch and Dunand [11] at ambient temperature. Both effects are captured by FEM, as discussed below.

5.2. Finite-element model—effect of stress

To date, models for creep in metallic foams consider beam deformation in a cellular architecture as the basic deformation mechanism, which has been described by continuum mechanical equations [14,19,20–26] or by FEM [15,27,28]. This approach cannot be used for syntactic foams because they do not contain the beams found in cellular, reticulated foams considered in the above models. For syntactic foams, pores are closed and surrounded by stiff, non-creeping shells, and deformation occurs in the creeping metallic matrix surrounding the hollow microspheres. This architecture is similar to that found in metal matrix composites containing non-hollow particles, for which the FEM approach has been successful to describe creep deformation [29–32]. However, very few FEM studies have investigated mechanics of syntactic metallic foams [33,34] and none have done so at elevated temperature, to our knowledge.

The present FEM model captures qualitatively the primary, secondary and tertiary stages observed experimentally (Figs. 2 and 5, respectively). The secondary creep rates determined for all calculated creep curves (shown in Fig. 5) are plotted in Fig. 6 for the FCC arrangement (due to limited computational time and resources, the effect of stress on the strain rate of the PR model was not investigated). This minimum strain rate determined by FEM exhibits the same trends as found experimentally for the syntactic foams: for lower stresses, the apparent stress exponent is close to unity, whereas for higher stresses, it is close to 13. Furthermore, the critical stress at which the stress exponent changes is quite well predicted: ∼11 MPa for the calculated FCC foams as compared to ∼8 MPa for the experimental syntactic foams. Due to periodic boundary conditions and the lack of direct contact between spheres, using the PR rather than the FCC structure does not noticeably improve the accuracy of the calculations. FE calculations with higher number of elements were attempted but could not be carried out to long enough creep times due to hardware limitations. It is thus likely that the current predictions for minimum strain rates carry large errors, but the goal of the modeling is to provide a qualitative comparison with data only. Furthermore, the variation of sphere diameters and wall thicknesses in real foams and the complex sphere spatial arrangements (including sphere-to-sphere contacts) prevent a direct quantitative comparison between FEM results and

experimental results, also given the broad range of volume fractions (f = 59–71% for the experimental foams as compared to the model (f = 65%). The relatively good match between model and experiments for both creep curves (Figs. 2 and 5) and stress sensitivity of strain rate (Fig. 6) may thus be somewhat fortuitous, but we believe it is a reflection of the fact the models capture the fundamental aspects of creep deformation of syntactic foams, including load transfer and the highly inhomogeneous stress distribution in the creeping matrix, as discussed below.

In unreinforced metals and alloys, a low-stress exponent close to unity is typical of Newtonian flow associated with diffusion-controlled creep and superplastic deformation. Here, however, the foam matrix deforms by power-law dislocation creep with a stress exponent n = 4.4, both in the FEM simulations (as specified in the model) and in the experiments. The latter can safely be assumed, since the foams have very coarse grain size (expected from the casting process) and the contribution of matrix/particle interfacial sliding can be assumed to be insignificant, due to the large size of the spheres and the expected good bonding between the aluminum matrix and the silica-mullite spheres. Thus, the low value of the apparent stress exponent corresponds to a dynamical steady state between continuously evolving load transfer between matrix and spheres, matrix stress concentrations and spatial distribution of spheres and matrix. For higher stresses, the apparent stress exponent (n = 14) is much higher than that of the matrix (n = 4.4), as also observed in many aluminum-based metal matrix composites [35,36] where it is often interpreted as a threshold stress. Here, there is no microscopic mechanism for a threshold stress, and the high apparent stress exponent is again due to a complex dynamic steady state. Thus, for both low- and high-stress regimes, the deviation of the foam stress exponent from the matrix value (n = 4.4) is not the result of a new mechanism (diffusional creep or threshold stress), but rather a result of load transfer varying with time and strain.

5.3. Finite-element model—stress distribution

The FEM results were further analyzed by determining the matrix stress distribution during a simulated creep test. The creep curve for a stress of 14 MPa, shown in Fig. 5, is reproduced in Fig. 7(a), to allow a better visualization of the primary, secondary and tertiary characteristic deformation stages and to show the seven different points where the equivalent von Mises stress distribution in the matrix was determined according to the following procedure:

- The von Mises stress for each matrix element was calculated as the mean of the values for the four individual integration points included in a tetrahedral element (integration point gives the most accurate value for the element stress).
- For each element, the volume was calculated, allowing binning of stress interval into a histogram representing the volume fraction of matrix whose von Mises stress is included in a given stress interval.
- Volume fractions f_i are calculated as the sum of the volume of all matrix elements with a von Mises stress between σ_i
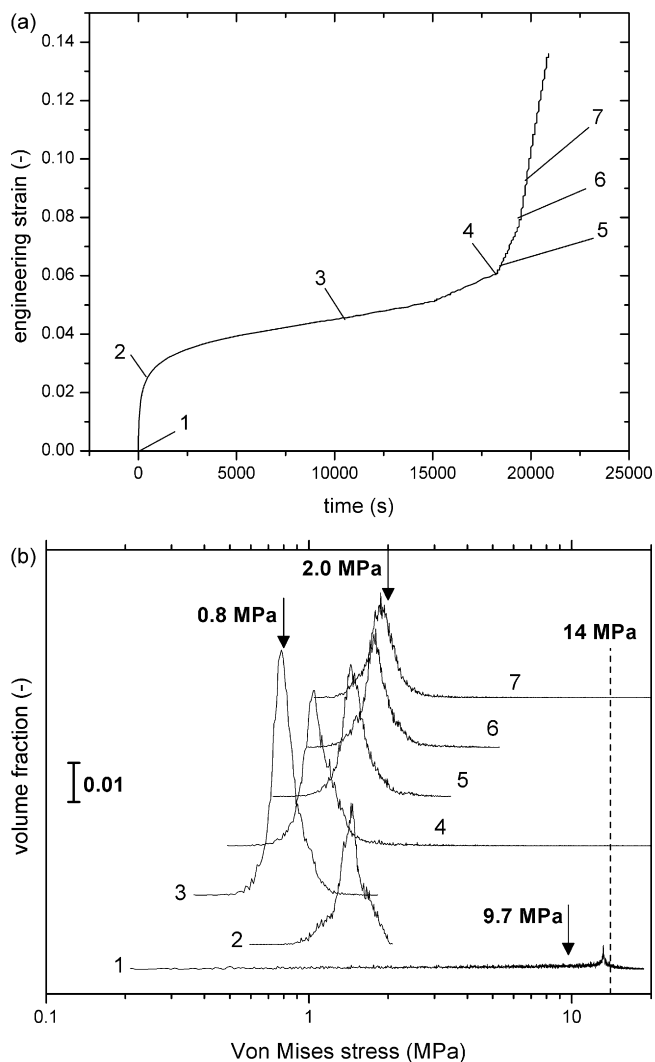
Fig. 7. (a) Creep strain as a function of time as calculated from FEM for FCC sphere arrangement ($f = 65\%$) deformed at $500\,^\circ$C under 14 MPa stress; (b) corresponding von Mises stress distribution in the matrix, calculated at seven creep strains labeled in (a). The volume average von Mises stress is indicated for histograms 1, 3 and 7. The applied stress is marked with a vertical dotted line.

and $\sigma_i + \Delta\sigma$ (where $\Delta\sigma = 0.1$ MPa) normalized by the total volume of the matrix.

Stress distribution histograms (plots of volume fraction f_i versus von Mises stress in the matrix) are shown in Fig. 7(b) for the seven points along the creep curve shown in Fig. 7(a). For the sake of clarity, the histograms are shifted along the volume fraction axis. Immediately upon loading (histogram 1 in Fig. 7(b)), the matrix volume average von Mises stress is 9.7 MPa. This is lower than the uniaxial applied stress of 14 MPa, indicating that elastic load transfer occurs from matrix to the hollow spheres, as modelled by Balch and Dunand [11] based on the enhanced stiffness of syntactic foams as compared to foams without ceramic hollow spheres.

After a short creep time interval in the primary stage (histogram 2 in Fig. 7(b)), the matrix volume average stress has dropped to 1.5 MPa, reflecting considerable further load trans-

fer from matrix to spheres as a result of matrix creep. The stress distribution has also narrowed (with most of the matrix exhibiting stresses between 1 and 2 MPa), indicating that relaxation of matrix areas with locally high stresses has occurred.

In the secondary creep stage (histogram 3 in Fig. 7(b)), the matrix volume average stress further decreases to a value of 0.8 MPa, indicating that the vast majority of the applied load is carried by the stiff, non-creeping hollow spheres. Only one histogram (histogram 3) corresponding to the secondary creep stage is shown in Fig. 7(b), but histograms were calculated over the whole secondary stage and the volume average von Mises stress remained constant within a 0.1 MPa variation. This further confirms that a quasi-steady state is achieved during creep deformation in the secondary creep stage.

At the onset of the tertiary stage, stress increases significantly in the matrix over a very short period of time (<10 s), as illustrated in histogram 4 in Fig. 7(b)). Elements with stress values as high as 100 MPa appear, and are located in the thin matrix regions separating the spheres. In the tertiary stage (histograms 5–7), the volume average matrix stress increases steadily as these stress concentrations become more pronounced and the overall foam strain increases.

In summary, the FEM analysis indicates that stress concentrations, initially present upon elastic loading due to the elastic mismatch between matrix and spheres, become attenuated during the primary creep stage due to localized matrix creep. This leads to a long period of secondary creep with low matrix volume average stress and little stress concentration. The tertiary creep stage is related to the re-appearance of sharp stress concentrations in the matrix, resulting in rapid localized matrix deformation. This scenario provides some guidance for the design of syntactic foams optimized to delay the onset of tertiary creep (leading to failure): these foams should display an architecture minimizing matrix stress concentrations, e.g., by using spheres with smooth surfaces and uniform sizes and spacings. The arrangement, stiffness, connectivity and coordination number of the spheres are also important parameters to take into account.

6. Conclusions

Syntactic foams, consisting of hollow ceramic microspheres in an aluminum matrix, were subjected to uniaxial compressive stresses at elevated temperatures. As expected from their high compressive strength and stiffness previously observed at room temperature [10,11], the foams are exceptionally creep resistant at $500\,^\circ$C as compared to reticulated foams without ceramic shells with the same density. All creep curves exhibit a primary stage where the strain rate decreases, followed by a secondary stage where the strain rate is minimum, and, at high stresses, a tertiary stage where the strain rate increases. In the secondary stage, the apparent stress exponent is close to unity for stresses below ~8 MPa, increasing abruptly to ~14 for higher stresses. FEM gives results which are in qualitative agreement with experimental strain rates.

FEM also sheds light on the details of creep deformation occurring in the matrix of these syntactic foams. In the primary

stage, the average matrix stress as well as stress concentration created during elastic loading of the foam decrease as a result of matrix creep and the resulting load transfer to the ceramic spheres. The secondary stage is characterized by low matrix stresses and stress concentrations. The tertiary stage appears due the re-emergence of stress concentrations in the matrix volume between spheres, resulting in a steady increase in the share of the load carried by the matrix.

Acknowledgements

References

[1] L.J. Gibson, M.F. Ashby, Cellular Solids, Structure and Properties, 2nd ed., Cambridge University Press, Cambridge, UK, 1997.
[2] R.Q. Guo, P.K. Rohatgi, Metall. Mater. Trans. B 29 (1998) 519.
[3] P.K. Rohatgi, R.Q. Guo, H. Iksan, E.J. Borchelt, R. Asthana, Mater. Sci. Eng. A 244 (1998) 22.
[4] M. Kiser, M.Y. He, F.W. Zok, Acta Mater. 47 (1999) 2685.
[5] N. Gupta, Kishore, E. Woldesenbet, S. Sankaran, J. Mater. Sci. 36 (2001) 4485.
[6] J. Bienias, M. Walczak, B. Surowska, J. Sobczak, J. Optoelectron. Adv. Mater. 5 (2003) 493.
[7] A.H. Brothers, D.C. Dunand, Appl. Phys. Lett. 84 (2004) 1108.
[8] E. Gikunoo, O. Omotoso, I.N.A. Oguocha, J. Mater. Sci. 40 (2005) 487.
[9] P.K. Rohatgi, J.K. Kim, N. Gupta, S. Alaraj, A. Daoud, Compos. Part A: Appl. Sci. Manuf. 37 (2006) 430.
[10] D.K. Balch, J.G. O'Dwyer, G.R. Davis, C.M. Cady, G.T. Gray III, D.C. Dunand, Mater. Sci. Eng. A 391 (2005) 408.
[11] D.K. Balch, D.C. Dunand, Acta Mater. 54 (2006) 1501.
[12] R.A. Palmer, K. Gao, T.M. Doan, L. Green, G. Cavallaro, Mater. Sci. Eng. A 464 (2007) 85.
[13] G.H. Wu, Z.Y. Dou, D.L. Sun, L.T. Jiang, B.S. Ding, B.F. He, Scripta Mater. 56 (2007) 221.
[14] E.W. Andrews, L.J. Gibson, M.F. Ashby, Acta Mater. 47 (1999) 2853.
[15] A.M. Hodge, D.C. Dunand, Metall. Mater. Trans. A: Metall. Mater. 34A (2003) 2353.
[16] D. Hibbitt, B. Karlsson, P. Sorensen, ABAQUS Standard v6.5.
[17] T. Miyoshi, M. Itoh, S. Akiyama, A. Kitahara, Adv. Eng. Mater. 2 (2000) 179.
[18] H. Frost, M. Ashby, Deformation-Mechanism Maps: The Plasticity and Creep of Metals and Ceramics, Pergamon Press, Oxford, 1982.
[19] E.W. Andrews, J.-S. Huang, L.J. Gibson, Acta Mater. 47 (1999) 2927.
[20] A.C.F. Cocks, M.F. Ashby, Acta Mater. 48 (2000) 3395.
[21] E.W. Andrews, L.J. Gibson, Mater. Sci. Eng. A 303 (2001) 120.
[22] P. Zhang, M. Haag, O. Kraft, A. Wanner, E. Arzt, Philos. Mag. A: Condens. Matter Struct. Defects Mech. 82 (2002) 2895.
[23] M. Haag, A. Wanner, H. Clemens, P. Zhang, O. Kraft, E. Arzt, Metall. Mater. Trans. A 34 (2003) 2809.
[24] H. Choe, D.C. Dunand, Mater. Sci. Eng. A 384 (2004) 184.
[25] M. Hakamada, T. Nomura, Y. Yamada, Y. Chino, Y.Q. Chen, H. Kusuda, M. Mabuchi, Mater. Trans. 46 (2005) 1677.
[26] J.Y. Lin, J.S. Huang, Compos. Sci. Technol. 66 (2006) 51.
[27] S.M. Oppenheimer, D.C. Dunand, Acta Mater. 55 (2007) 3825.
[28] W.S. Sanders, L.J. Gibson, Mater. Sci. Eng. A 347 (2003) 70.
[29] P. Sofronis, R.M. McMeeking, Mech. Mater. 18 (1994) 55.
[30] S.L. Atkins, J.C. Gibeling, Metall. Mater. Trans. A 26 (1995) 3067.
[31] L.C. Davis, J.E. Allison, Metall. Mater. Trans. A 26 (1995) 3081.
[32] L.G. Lim, F.P.E. Dunne, Int. J. Mech. Sci. 38 (1996) 19.
[33] M.Y. He, B. Wu, F.W. Zok, Mech. Mater. 20 (1995) 315.
[34] M.Y. He, M. Kiser, B. Wu, F.W. Zok, Mech. Mater. 23 (1996) 133.
[35] Y. Li, T.G. Langdon, Acta Mater. 45 (1997) 4797.
[36] F.A. Mohamed, Mater. Sci. Eng. A 245 (1998) 242.